Journal of Structural Geology 30 (2008) 791–808

Contents lists available at ScienceDirect

Journal of Structural Geology

journal homepage: www.elsevier.com/locate/jsg

Crack formation on top of propagating reverse faults of the Chuculay Fault System, northern Chile: Insights from field data and numerical modelling

Gabriel González [a,*], Muriel Gerbault [b], Joseph Martinod [c], José Cembrano [a], Daniel Carrizo [a], Richard Allmendinger [d], Jacob Espina [a]

[a] Departamento de Ciencias Geológicas, Universidad Católica del Norte, Avenida Angamos 0610, Antofagasta, Chile
[b] IRD, Departamento de Geología, Universidad de Chile, Plaza Ercilla 803, Santiago, Chile
[c] Laboratoire des Mécanismes de Transfert en Géologie (LMTG), Université de Toulouse, France
[d] Department of Earth and Atmospheric Sciences, Cornell University, Ithaca, NY 91125, USA

ARTICLE INFO

Article history:
Received 29 March 2007
Received in revised form 25 January 2008
Accepted 4 February 2008
Available online 4 March 2008

Keywords:
Reverse faults
Fractures
Fault scarps
Numerical modelling
Northern Chile

ABSTRACT

Reverse faults in northern Chile have formed 20–300 m high scarps that contain open fractures which occur in a zone of 20–1600 m wide. Two-dimensional numerical models were used to explore the geometrical and mechanical parameters needed to produce extension within a bulk contractional regime. All of the mechanical models show the same structure as the field: a concentration of cracks predominantly at the top, rather than on the forelimbs of the scarps. In the field case extension begins as soon as a discrete scarp forms; with progressive shortening the scarp height increases producing a broadening of the zone in extension. The numerical models show that this broadening stabilizes when a maximum in the scarp height is reached. To produce concentration of the extension on top of the scarps, the reverse fault needs to be weak ($\phi \sim 10^{\circ}$). The models suggest that distribution of this extensional zone depends on the cross-sectional geometry of the fault and on the location of the detachment at depth. The main mechanism that produces extension on the top of the reverse scarp is stretching of the topographic surface by folding of the hanging wall at the tip of the fault zone.

1. Introduction

Cracks related to fault propagation have been widely reported in the literature. Their most common occurrence is in strike-slip faults where en-echelon cracks are characteristic at releasing bends, at extensional step-overs or ahead of tip lines of propagating strike-slip faults (Tchalenko, 1970; Klinger et al., 2005). Crack occurrence related to propagation of dip-slip faults has also been documented (Yielding et al., 1981; Hilley et al., 2001; Rajendran et al., 2001; Martel and Langley, 2006). For example, blind normal faults frequently form monoclines with secondary tensional structures on the crest. These structures, including cracks and secondary normal faults, are parallel to the strike of normal faults. Similarly oriented extensional structures have been observed to form coseismically during large historical thrust-fault earthquakes. King and Vita-Finzi (1980) documented open cracks and normal faults that formed during the 1980 El Asnam, Algeria reverse-fault earthquake. In this case, extensional structures formed on top of uplifted blocks (Philip and Meghraoui, 1983).

Numerous analogue and numerical models based on rock mechanics have simulated fault structures developing in a crustal layer under compression (e.g. Hafner, 1951; Jaeger and Cook, 1979; Malavieille, 1984; Sassi and Faure, 1997). These models help to understand the first-order relationship between fault-propagation fold geometries and the amount of slip on master faults (Allmendinger, 1998; Cardozo et al., 2003; Mitra and Islam, 1994; Finch et al., 2003), but the relationship between secondary tensional structures (cracks and normal faults) and reverse-fault propagation remains poorly understood. Healy et al. (2004) performed elastic models to predict the mode and distribution of subseismic fractures around large reverse earthquakes, using as natural setting the El Asnam, Algeria earthquake. Comparison between models and the natural examples helps to understand critical geometrical parameters of a scarp able to produce extensional structures on top of propagating reverse faults. Furthermore, numerical models allow unravelling the mechanical properties of faults and their mechanical contrast with deforming rocks at the scale of hundreds of meters.

Near the Salar Grande in northern Chile (21°05′–21°15′), a conspicuous network of open cracks pervades the topographic surface. These cracks occur at the top of, and strike parallel to, 20–300 m high reverse-fault scarps, suggesting that their origin is causally

* Corresponding author. Tel.: +56 55 355952; fax: +56 55 355977.
E-mail address: ggonzale@ucn.cl (G. González).

0191-8141/$ – see front matter © 2008 Elsevier Ltd. All rights reserved.
doi:10.1016/j.jsg.2008.02.008

connected with either fault propagation or collapse of these fault scarps. Due to the hyper-arid conditions of the Atacama Desert, these open fractures are extremely well preserved and constitute a superb example of secondary structures related to reverse faulting. Using 1 m spatial resolution IKONOS satellite imagery, we mapped 16,358 fractures over a 250 km^2 area. Integrating the IKONOS data with 90 and 20 m resolution DEMs, we describe the general geometry of the fractures and their spatial relationship with the fault scarp. Geological observations help to characterize some attributes of the fractures in the field. In the second part of this paper we use numerical models to reproduce extensional zones on top of developing reverse faults. By comparing data and models, we constrain the origin of the fractures and delineate some geometrical parameters and mechanical properties of the deforming rocks and the fault zone.

2. Tectonic setting and topography of the Central Andes forearc

The tectonic setting of the study area is dominated by the subduction of the Nazca Plate beneath the South American Plate (Fig. 1). The interplate seismogenic zone (Tichelaar and Ruff, 1991) extends offshore and below the coastal line of Peru and Chile. Several thrusting earthquakes, 40 and 50 km below the Coastal Cordillera, define the seismic coupling zone of the Andean subduction zone (Delouis et al., 1996; Comte et al., 1999).

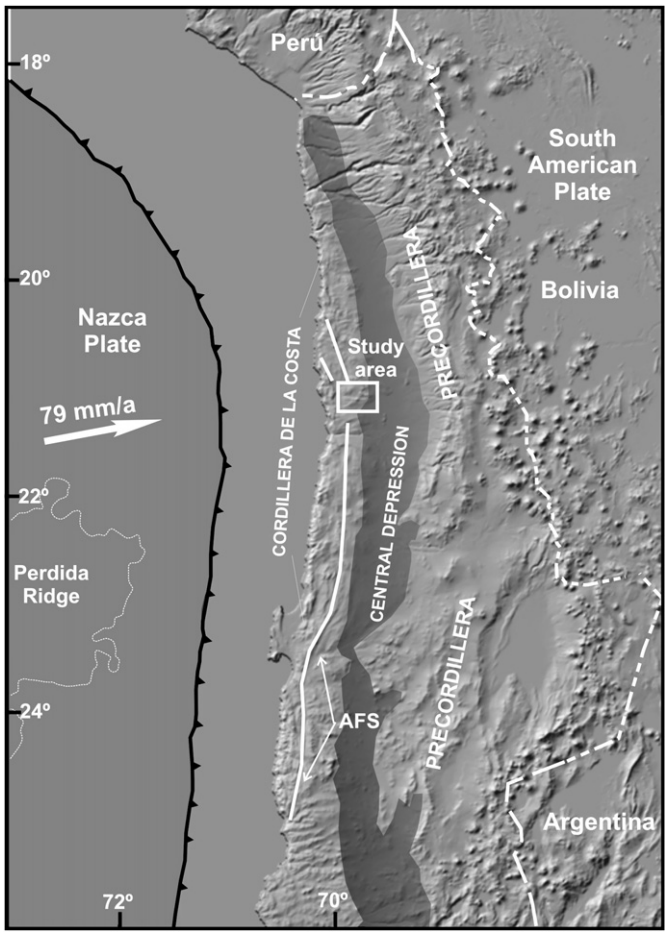

Fig. 1. Tectonics and morphology of the western border the Central Andes, showing the main morpho-structural units of the Coastal Cordillera, Central Depression and Precordillera. The polygon shows the location of the study area. Onshore digital topography from the USGS 30″ DEM.

The topography of the Central Andes forearc is composed of three morpho-structural units, the Coastal Cordillera, the Central Depression and the Precordillera (Fig. 1). The Coastal Cordillera is a structural height, located 1000–2000 m above sea level; the western margin is formed by ~1000 m of a high sea cliff which dominates the topography of the coastline (Fig. 2). The eastern side of the Coastal Cordillera is a smooth and gradual boundary with the Central Depression. The top of the Coastal Cordillera is a 20 Ma old pediplain surface (Dunai et al., 2005; Carrizo et al., 2008). The preservation of this surface testifies to the long-term dominance of the hyper-arid climate in the Atacama Desert.

3. Structural framework of the area

The study area is located within the Coastal Cordillera, between 21°05′S and 21°15′S. The structural framework is highlighted by spectacular morphological expression of NW and ENE to E–W striking faults (Fig. 2). The most important NW-striking fault is the Salar Grande Fault which produces a 30–40 m high scarp on the halite surface of the Salar Grande. Along the northernmost part of the Salar Grande Fault several valleys crossing the trace show dextral offsets documenting a strike-slip component for the fault (González et al., 2003; Carrizo et al., 2008). Another important NW-striking fault is the Chomache Fault, located west of the Salar Grande. Several stream channels flowing across the fault also show dextral offsets. E–W structures are regionally visible across the Coastal Cordillera, between 22° and 20°S. They are displayed in the 90 m DEM as several scarps that extend from the coastal line to the eastern side of the Coastal Cordillera (Fig. 2). The scarps end at the boundary between the Coastal Cordillera and the Central Depression, terminating in fault-propagation folds that affect the Tertiary infill of the Central Depression (Allmendinger et al., 2005). The lack of horizontal offset of paleovalleys crossing the scarps documents predominantly dip-slip displacement.

Exposures of the fault plane of the E–W faults are very scarce, the few documented cases show consistently that the fault planes dip beneath the uplifts (Allmendinger et al., 2005), confirming that the scarps were formed by displacement of the topographic surface by slip along reverse faults. On closer inspection, it is clear that some scarps are associated with emergent reverse faults that offset the topographic surface, whereas other scarps result from folding of the surface above blind reverse faults. Regionally, the youngest known motion for these faults is documented by vertical offset of the Late Pleistocene (younger than 125 ka) coastal terrace exposed at the base of the Coastal Escarpment (Fig. 4a, Caleta Chica 19°20′, Iquique 20°17′ and Barranco Alto 20°38′). In general, fault planes dip to the north or south, with dip angle being steeper (~68°) in the higher parts of the Coastal Cordillera and gentler at sea level (~30°). Combined with the 1–4° rotation of the paleosurface, this suggests that the fault planes are listric. Furthermore, some of the E–W thrust-faults are reactivated Mesozoic normal faults. In fact, close to Caleta Chica, an E–W reverse fault places Early Cretaceous conglomerate over Jurassic volcanic rocks of La Negra Formation. This geometry clearly suggests inversion of a Mesozoic rift basin. Other field evidence, in the form of small scarps localized at the foot of the highest scarps (Fig. 3c), indicates that the E–W fault scarps were formed by successive discrete slip events.

4. The Chuculay Fault System

East of the Salar Grande, the most relevant structures are ENE to E–W striking reverse faults, which are collectively known as the Chuculay Fault System (Allmendinger et al., 2005). These faults control the topography, forming five 20–300 m high north-facing scarps (Figs. 3 and 4). The scarps extend from the eastern margin

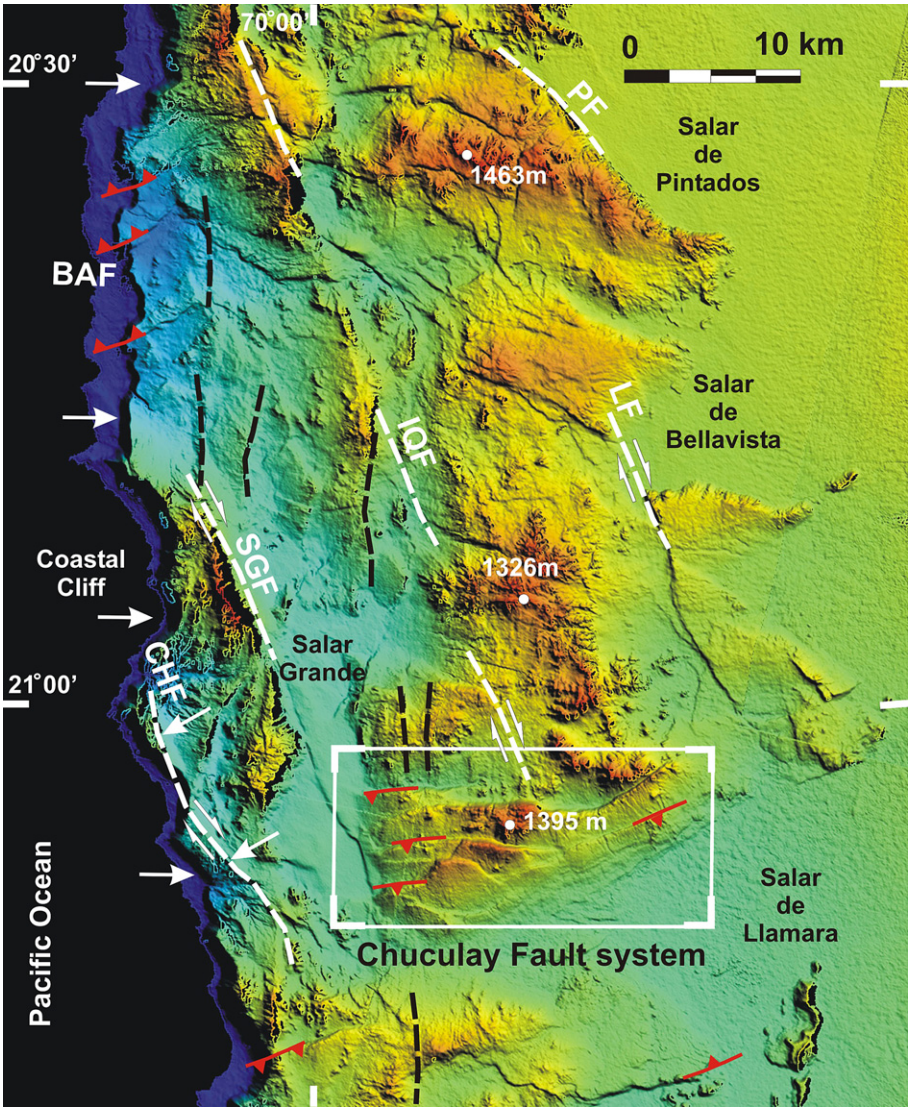

Fig. 2. Shaded relief map of northern Chile based on the new Shuttle Radar Topographic Mapping Mission 90 m DEM of northern Chile. The main NW dextral faults are shown with white colour segmented lines. The E–W reverse faults are shown with red lines. The polygon shows the location of the study area. BA = Barranco Alto Fault, CHF = Chomache Fault, SGF = Salar Grande Fault, IQF = Iquique Fault, LF = Lagunas Fault, and PIF = Pintados Fault. (For interpretation of the references to colour in this figure legend, the reader is referred to the Web version of this article.)

of the Salar Grande to the eastern border of the Coastal Cordillera, defining a 25 km long and 15 km wide fault system (Fig. 4). The scarps were formed in Mesozoic dioritic and andesitic rocks (La Negra Formation, García, 1967) which are covered by Tertiary colluvial and alluvial sediments. These sediments form part of a relict piedmont whose topographic heights are localized in the central and eastern parts of the Chuculay area (Figs. 2 and 4). Inactive drainages arising from the topographic culmination are cut and displaced down slope in the footwall of the reverse faults. The more distal part of the drainages is uplifted in the hanging wall showing that the reverse displacement has a dominant north vergence.

Because topographic denudation has been particularly small during the last 20 Ma (Dunai et al., 2005), fault plane exposures are scarce. The few outcrops in the Chuculay area are confined close to the eastern tip line of the northernmost fault of the Chuculay Fault System (fault FA in Fig. 4). There, beneath the north-facing scarp Allmendinger et al. (2005) described a fault plane dipping 60–68° to the south. The fault plane contains down-dip striae and kinematic indicators that indicate pure thrust displacement.

4.1. Scarp morphology

Because the open fractures are spatially related with the Chuculay Fault System we describe its morphology in some detail. The general morphology is characterized by southward tilted blocks with steep frontal limbs facing to the north and gentle back limbs dipping 2.5–4.4° to the south (Fig. 4). The scarp profiles change systematically with the emergent or blind character of the fault. Where the fault cuts the surface, scarp profiles are steeper (~40°), higher (~250 m) and crystalline rocks are exposed on the upper part of the scarp (Fig. 5a). Where the fault is blind, the scarp profile is gentler (~15°) and lower (<50 m); forelimb and back limb form a single folded surface, and no crystalline rocks are exposed at the slope of the scarp (Fig. 5b). Faulting and folding of the topographic surface affect some paleovalleys which run perpendicular to the scarp strike (Fig. 5b). Several 1–2 m high scarps are present at the foot of the main scarp (Figs. 3 and 5b). Trenches dug across these smaller scarps demonstrate that low angle reverse faults have propagated from the base of the major scarps.

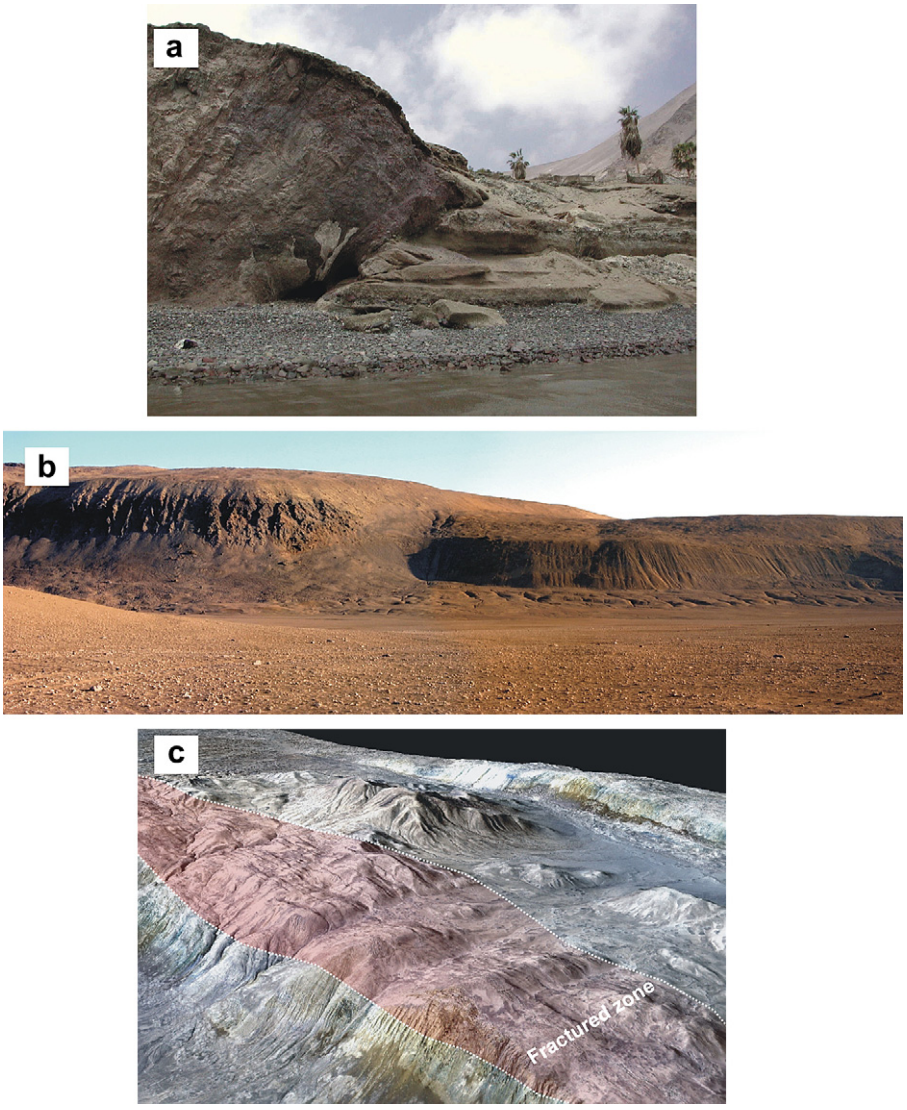

Fig. 3. Field photos showing E–W faults and fault scarps. (a) Coastal outcrops showing Jurassic volcanic rocks thrusted on Late Pleistocene marine sediments, view to the east. (b) Composite scarp showing small reverse offset at the base of the 80 m high scarp (Fault C). (c) Oblique view of IKONOS image showing the scarp of Fault B to the south. See the fracture zone localized on top of scarp.

^{21}Ne exposure ages of 24 Ma obtained in quartz clasts overlying abandoned alluvial surface in the hanging wall of the fault FA suggest that the propagation of these reverse faults started early in the Miocene (Carrizo et al., 2008). An age of 4 Ma obtained at the river bed of displaced drainages indicates that faults were active at least during the latter part of the Pliocene (Carrizo et al., 2008). ^{40}Ar/^{39}Ar analysis in biotite from tuff layers interbedded in the alluvial–colluvial sediments, which are cut by the reverse faults that formed the small scarps, gave an age of 0.3 ± 0.1 Ma. This youngest age shows that some reverse faults of the Chuculay Fault System remained active at least until the Middle Pleistocene, consistent with coastal exposures along other E–W faults.

5. Description of the cracks

The surface deformed by the Chuculay Fault System contains an anhydrite and gypsum-rich cohesive soil (gypcrete). The soil covers a large part of the landscape of the study area including mountain flanks, flat portions (pediplains) and paleovalleys; on the flats, the soil can reach up to 2 m thick. The cohesive character of the soil and the hyper-aridity environment prevailing in the study area allow an extremely quality preservation of the fractures. This gypsum-rich soil shows polygonal fractures that are not spatially related to fault scarps; they define meter wide polygonal blocks that form 2 cm deep depression on the topographic surface (Fig. 5b). These polygonal fractures are produced by volumetric changes related to hydration–dehydration processes of the soil (Tucker, 1978).

In contrast, fractures spatially related to fault scarps are parallel to the scarp trend (Fig. 6) and they do not show the distinctive polygonal character of soil fracture. Below, we name the fractures spatially related to fault scarps as "scarp cracks". This type of fracture is systematically present in the uplifted block of the scarps. Some scarp cracks are open and formed directly by fracturing of the crystalline rocks (Fig. 7a and b) whereas others are formed by fracturing of the gypsum soils (Fig. 7c and d). In the first case the cracks penetrate at least 12 m below the topographic surface. In the high resolution IKONOS data the scarp cracks show a typical zigzag appearance which is best expressed when the open fractures are developed in the bed rock. The length of the cracks measured in these images varies between 2 and 743 m with an average length of 100 m.

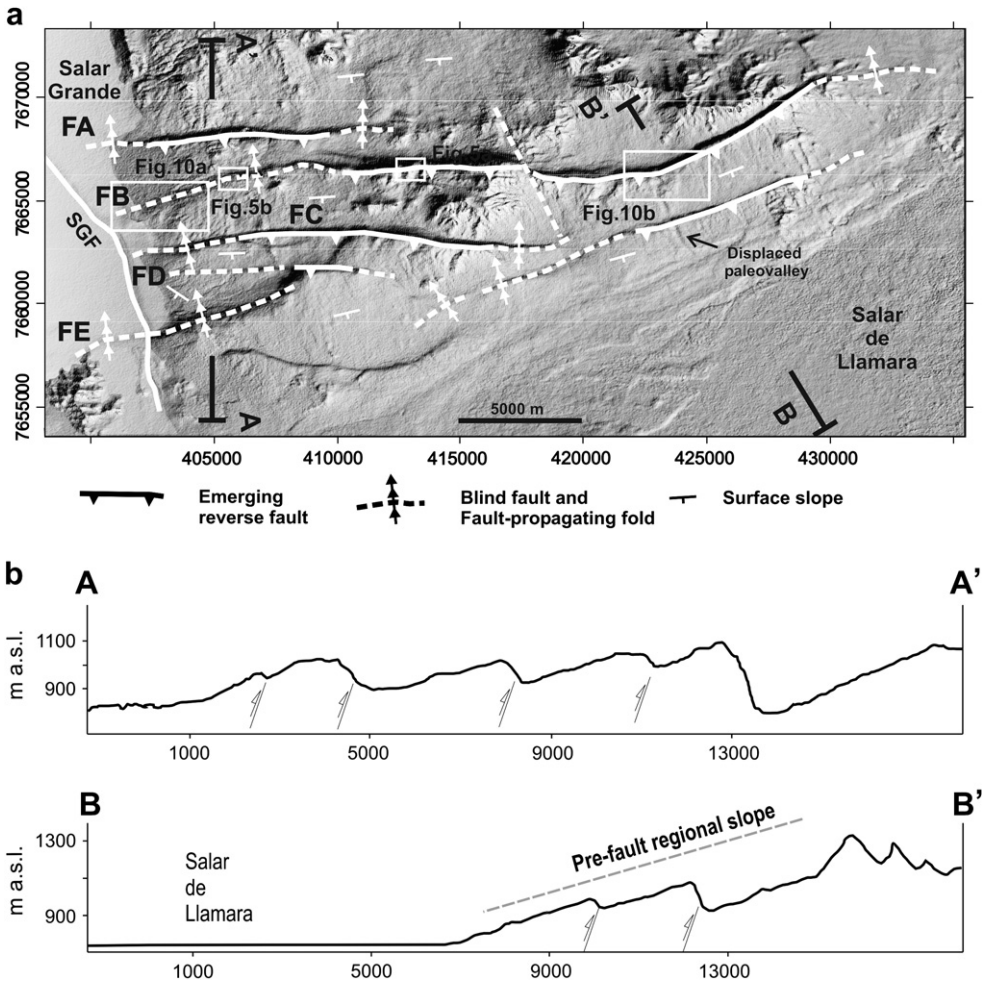

Fig. 4. (a) Shaded relief map of the Chuculay Fault System based on a 20 m resolution DEM. The main reverse faults controlling the topography are shown with white lines. (b) Topographic profiles constructed across the faults showing the tilted blocks affecting the mid-Tertiary erosion surfaces.

Fractures commonly have a salt-indurated, sandy infill attached to the fracture margins and an open central portion. Episodic fracture opening is suggested by internal, centimetre-scale banding in the infill which is parallel to the crack walls.

Fracture distribution is strongly correlated with the scarp's trend, forming fracture clusters close to the hinge zone of fault-propagating folds (Figs. 5 and 8). The width of the fractured zone above the scarps varies from 50 to 2000 m, being generally wider where the scarps are higher. Fig. 9 shows a linear correlation between the width of the fractured zone and the height of the scarp. However, close inspection of the 20 m resolution DEM highlights a couple of exceptions to this general relationship: in the first case, a wide fracture zone is located at the tip line of the Fault B. There, the cracks branch off from the tip point with fan geometry (Fig. 10a). The second case occurs along the same fault where a 1270 m wide zone of fractures is oriented obliquely with respect to the scarp trend (Fig. 10b). We interpret this wider extensional zone to be an inherited geometry which formed during the lateral propagation of the fault. Eastward lateral propagation of the fault captured this tip zone. This suggests that the reverse faults of the Chuculay Fault System formed by coalescence of juxtaposed segments which grew laterally and coalesced, forming a through-going linked reverse fault. In fact, we can identify 1 km long fracture segments which characteristically have, at their tips, branching crack zones. In these zones, extension is higher than the central part of the segment.

The central point of each digitalized fracture on the IKONOS data is referred to as the "centroid". We quantify the concentration of fractures by contouring the centroid density to explore the relationship between fracture distributions and topography. Fig. 8 shows that fracturing generally concentrates just above scarps. Fracturing of scarp slopes, in contrast, is modest. Moreover, the faulted pre-existing topographic heights for instance, do not concentrate superficial fractures. This is clearly visible in Fig. 8b, where the highest local topographic zones do not present any surface cracks. The last indicates that fractures are not produced by collapse of the topography, but rather by horizontal stretching of the scarp crest.

6. Extension related to fracture propagation

In order to determinate the fracture aperture in the field and the corresponding extensional strain, we mapped seven transects trending perpendicular to the strike of the fractures. All of these transects are localized above Fault B, close to the scarp crest (Fig. 4). Fracture aperture in these transects ranges from 0.1 to 6 m and has an average aperture of 1.3 m. Diffusion and slumping of the walls of the fractures increase the aperture produced by mechanical splitting of the rock mass (structural aperture). The superficial aperture (apparent aperture) enhanced by wall degradation, representing approximately 33% of the structural aperture (0.42 m in average). The extension related to crack formation along these seven transects varies from 0.8% to 4.4% (Fig. 11a). The total extension along these transects varies from 5 to 16 m. Additionally, using the IKONOS data set, we estimated the extension along 10

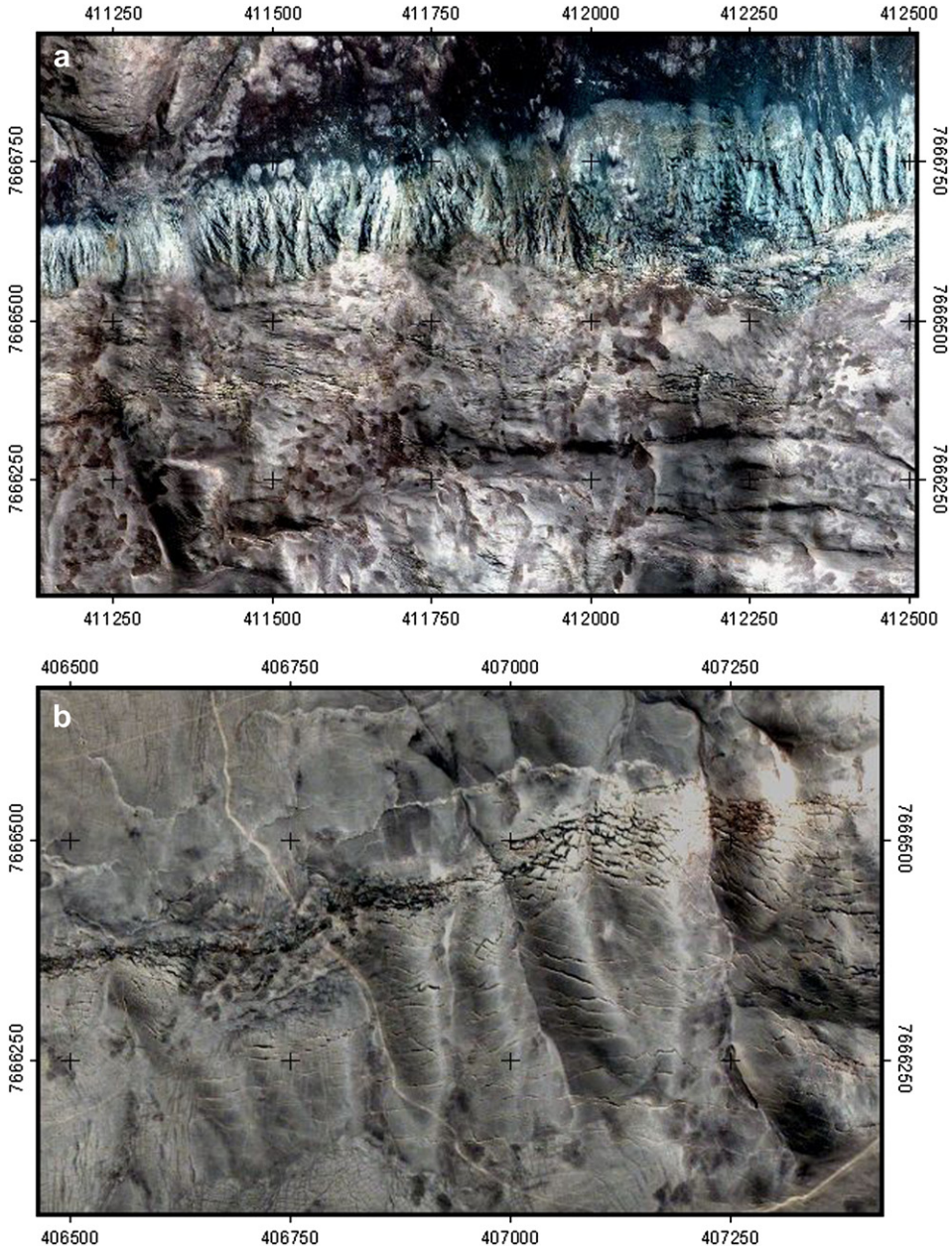

Fig. 5. (a) IKONOS image showing the emergent part of the Fault B and (b) IKONOS image showing the surface expression of the blind part of Fault B (see Fig. 3 for location). In (a) one can see two topographic surfaces: a smooth one offset by the fault and the slope of the scarp (rugged texture). On this latter surface, medium grained granodiorites are locally exposed on the uppermost part of the scarp. Talus breccias at angle of repose form the middle part of scarp and colluvial–alluvial deposits form the bottom of the scarp. Plutonic rocks are strongly chemically altered and intensively fractured, both related to salt penetration. In contrast, the scarp in (b) has smooth topography. The slope is ~10–20°, and the old surface forms a continuous surface covered by the saline soil. This soil is fractured close to the scarp. The intensely fractured area is not directly related to the topography: on the right side fractures are concentrated close the hinge zone, and on the left side they mainly appear on the scarp slope. In both figures, distance between tick marks is 250 m.

transects (total length is 19 km) by counting the fractures intersecting transects, and then we multiplied this value by the mean fracture aperture (0.42 m). Extension obtained using the IKONOS data set varies from 0.8% to 2.4%. The difference in extension between field and IKONOS data comes from the fact that field transects were located in areas that presented the larger and denser set of cracks.

7. Fracture mode and stress condition

Open cracks can be considered mode I tensile fractures that open perpendicular to the plane of the fracture at the fracture tip (Hancock, 1985). On the other hand, hybrid shear fracturing (under mode II) can produce opening of fractures by oblique slip with shear parallel to the fracture. Both types of fractures require tensile stress conditions, meaning that the minimum principal stress is negative ($\sigma_3 < 0$, using a geological sign convention). Mode I fractures form perpendicular to σ_3 and parallel to σ_1 whereas hybrid shear fractures form at an angle θ (see below) to the maximum principal stress.

Plumose structures with a central suture oriented vertical and parallel to the fracture plane indicate that most fractures formed by mode I rupture and propagated perpendicular to the surface. In this case, during crack formation σ_1 was oriented sub-vertical, and fracture planes parallel σ_1 and σ_2 axes of the stress ellipsoid. Because most of the scarp cracks are vertical, we can assume that

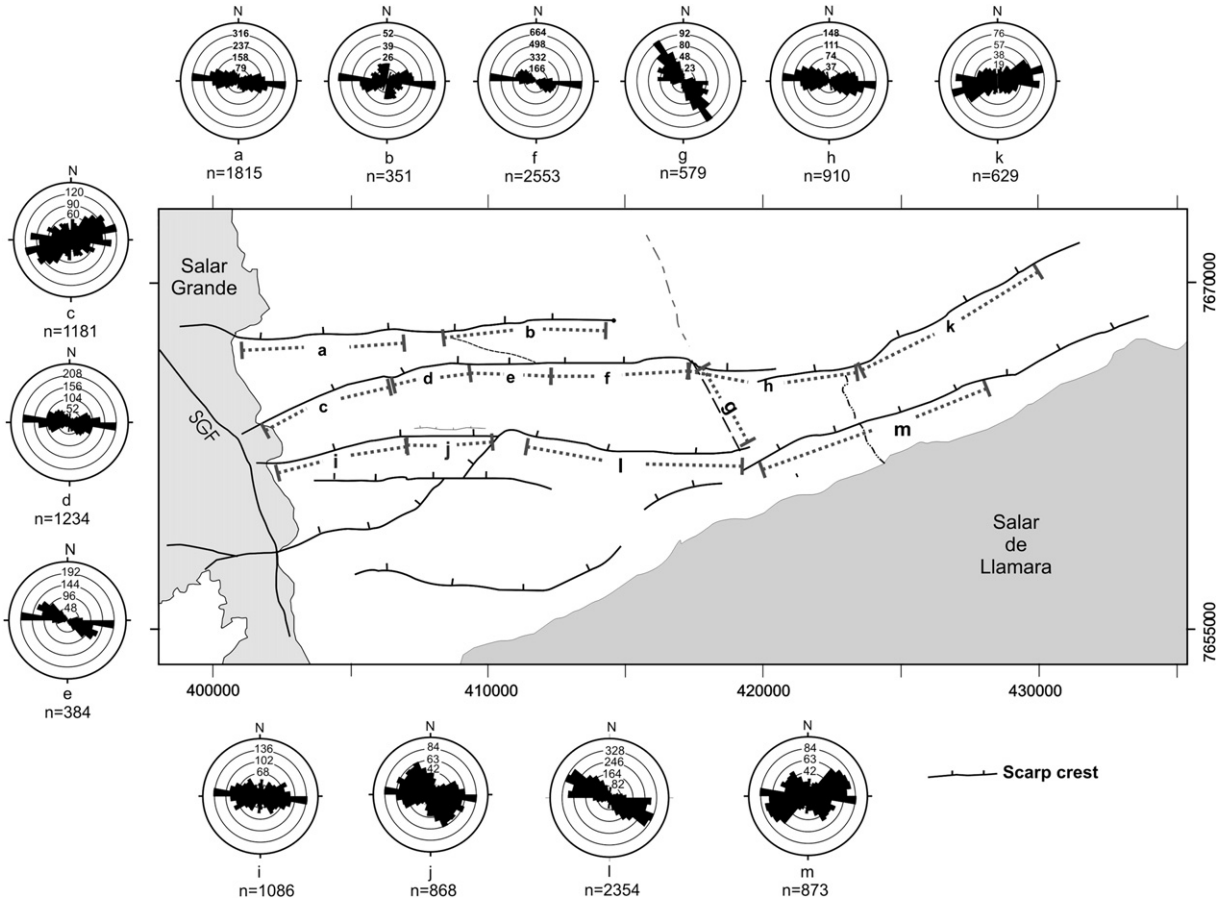

Fig. 6. Structural map of the Chuculay Fault System; rose diagram shows the orientation of the cracks above the reverse-fault scarp.

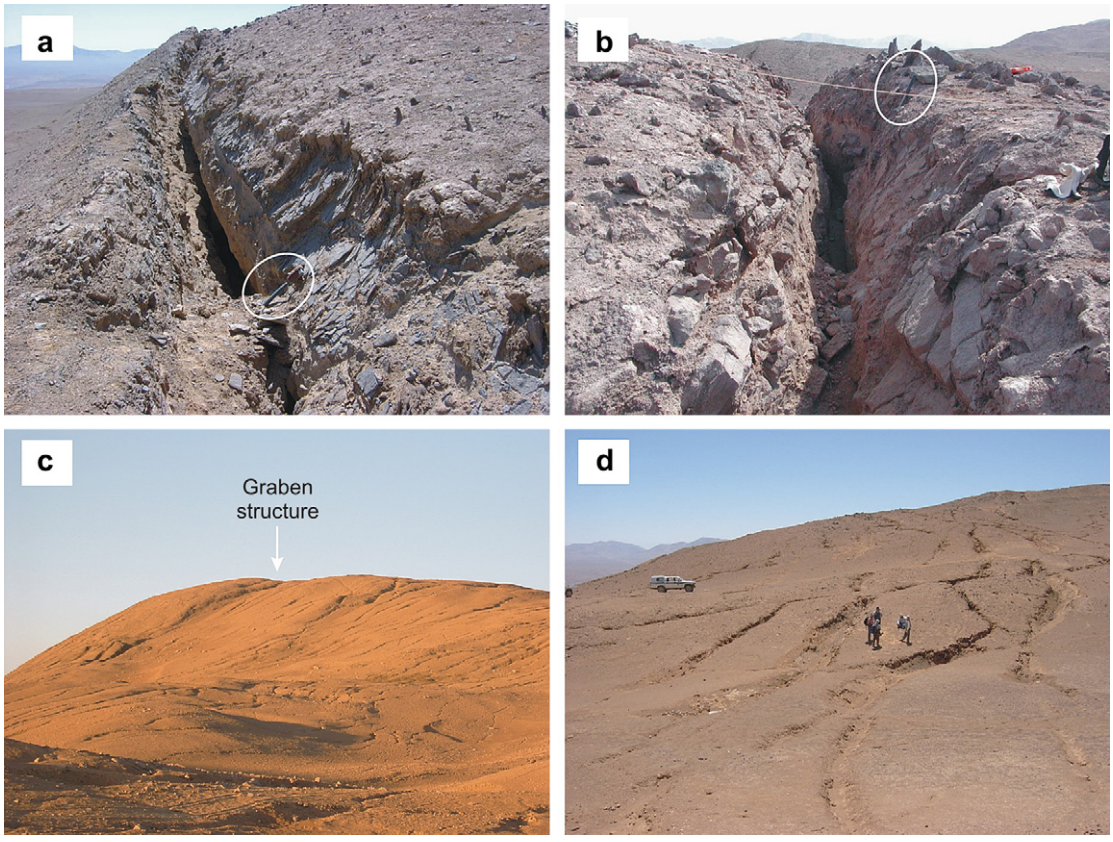

Fig. 7. Field photos of cracks located on top of the scarp of Fault B. (a) Cracks formed in Jurassic volcanic rocks, note the crack infill adhered to the side wall of the fracture. The central portion is open indicating a later reopening of the crack. (b) Cracks formed in volcanic rocks, these cracks penetrate at least 3 m below the topographic surface. (c, d) Network of cracks exposed above the scarp of the Fault B.

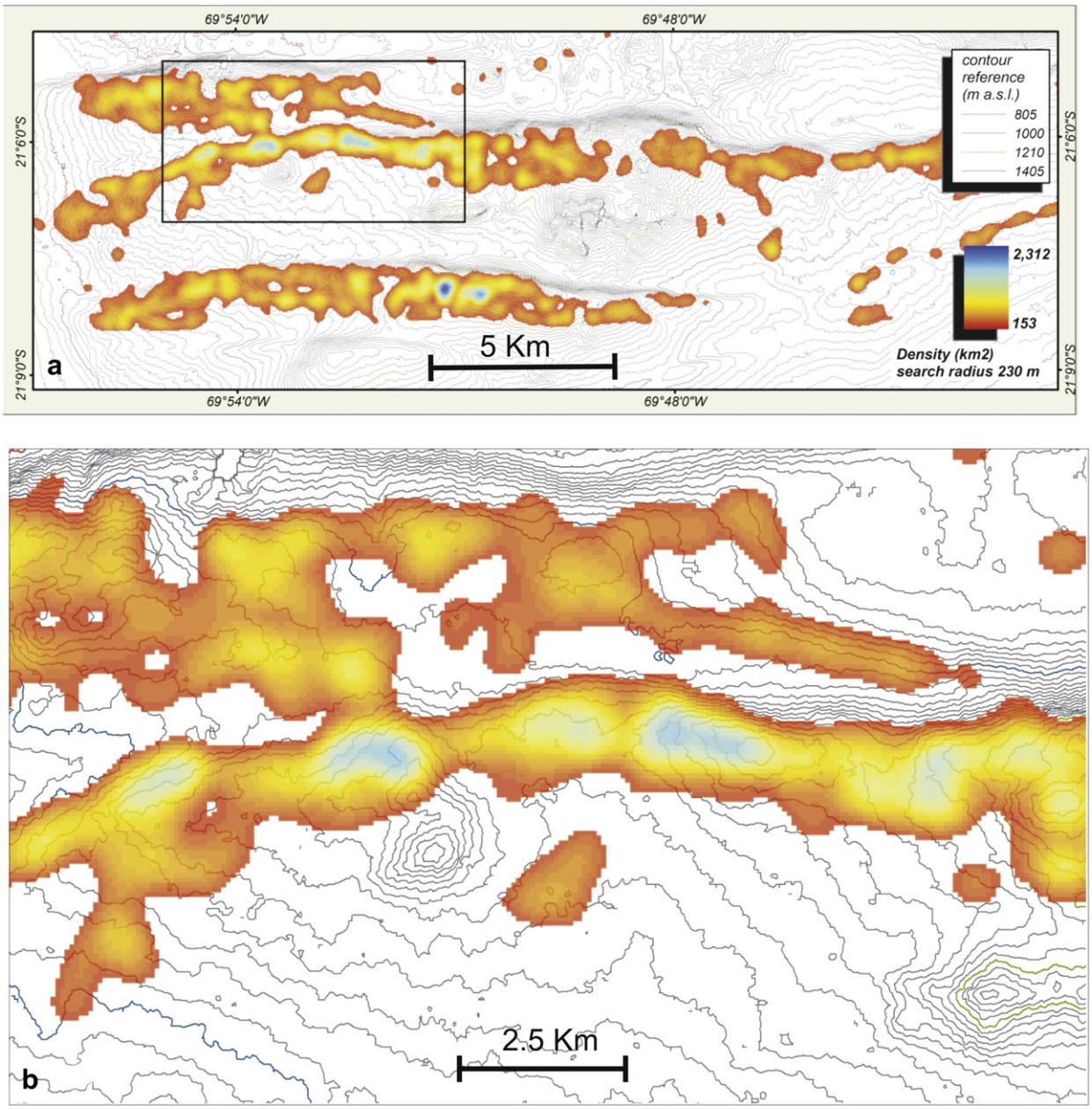

Fig. 8. (a) Distribution of fracture centroids and topography of the reverse-fault scarp; 50 m topographic contour interval. (b) Details of fracture centroid density. Note that high-density clusters; violet and blue colours are not exposed on the uppermost part of the topography; 15 m topographic contours.

poles of fractures represent the orientation of σ_3 and that fracture strikes represent the orientation of the intermediate stress. This superficial stress tensor above fault scarps contrasts with that prevailing at depth: within the crust, σ_1 is sub-horizontal and perpendicular to the fault scarps, and σ_3 is sub-vertical. Therefore, σ_1 and σ_3 principal stress axes shift when approaching to the surface of the fault scarps.

The fractures in the Chuculay Fault System were formed primarily as mode I cracks; only minor, crack parallel shear was involved. Along some segments of the fault scarp we observed hybrid shear-opening cracks in the forelimb; these fractures always have their uplifted side on the downhill side of the scarp indicating that fractures dip into the hinge zone of the fold-scarp. We suspect that these cracks initiate as mode I cracks and subsequently get sheared during folding. Locally, large vertical offsets up to 6 m are observed along normal faults occurring in the back limb of the 390 m high fault scarp, demonstrating that shear is involved in the evolution of these extensional structures.

8. Modelling fractures developing on top of the Chuculay Fault System

Numerical simulation of faulting in rocks is not trivial because it must account for the transition from initially continuous deformation, basically elastic, towards localized and thus discontinuous deformation that defines the brittleness of the fault itself. Several mechanical approaches have been developed to simulate the development of brittle faults in intact medium, using the continuum approach of solid mechanics. The simplest and oldest way has been to calculate the stress field by means of the theory of elasticity (e.g. Anderson, 1951; Hafner, 1951), where faults are predicted to occur at a certain angle from the direction of principal stresses when

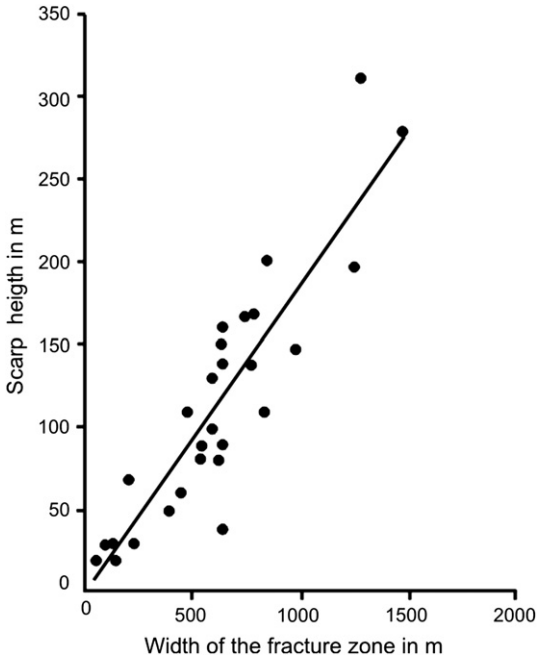

Fig. 9. Height of the scarp vs. width of the fractured zone. Note the linear correlation between parameters.

the condition for fault friction is satisfied. A more advanced approach involves the theory of metal plasticity, in which faults are interpreted as velocity discontinuities that control the motion of rigid blocks (e.g. Stockmal, 1983; Dahlen, 1984). The theory of non-associated elasto-plasticity is today, perhaps the most appropriate theory for fault prediction, but it has taken time to be developed and then accepted in geological analysis (e.g. Rudnicki and Rice, 1975; Vermeer and de Borst, 1984; Hobbs and Ord, 1989; Gerbault et al., 1998). In elasto-plasticity, the material first "loads" elastically, until the yield stress criterion for failure is reached, deformation then becoming permanent, evolving either in a diffuse or localized manner in space (shear bands are then assumed to represent faults).

We perform numerical models to unravel the driving geometrical and mechanical parameters that control the formation of the open fractures observed in the Chuculay Fault System. We used the finite difference code Parovoz (Poliakov and Podladchikov, 1992), a Fast Lagrangian Analysis of Continua (FLAC) method (Cundall and Board, 1988), using an explicit time-marching algorithm. Parovoz solves the equations of motion in large strain mode, retaining a locally symmetric small strain formulation commonly used in continuum mechanics. This method is well known to reproduce initialization and evolution of non-predefined faults (treated as shear bands, e.g. Poliakov and Podladchikov, 1992). The program executes for each time-step, the following procedure: velocities are first calculated from Newton's law, with density ρ, time t, velocity vector V, stress tensor σ, and gravity acceleration g:

$$\rho \delta V_i/\delta t = \delta \sigma_{ij}/\delta x_i + \rho g \tag{1}$$

where $\delta/\delta t$ and $\delta/\delta x_i$ are the time and space derivatives, respectively. The deformation rate is defined as

$$\dot{\varepsilon}_{ij} = 1/2\left(\delta V_i/\delta x_j + \delta V_j/\delta x_i\right) \tag{2}$$

and is used to calculate the new stress distribution from an elasto-plastic constitutive law. Nodal forces and displacements are evaluated and used for the next time-step.

We use mechanics stress convention, assuming that compressional stresses are negative and that the most compressive principal stresses are $\sigma_1 < \sigma_2 < \sigma_3$. Elasticity relates stress and strain with Lamé's parameters λ and G (δ_{ij} is the Kronecker delta):

$$\sigma_{ij} = \lambda \varepsilon_{ij} + 2G\varepsilon_{ij}\delta_{ij} \tag{3}$$

The Mohr–Coulomb failure criterion relates normal and tangential stresses, σ_n and τ, along any given orientation according to

$$\tau = \mathrm{So} - \tan\phi\sigma_n \tag{4}$$

So is cohesion and ϕ the internal friction angle. The dilatancy angle is set to 0, so that non-associated plastic flow occurs (Vermeer and de Borst, 1984). Non-associated plastic flow generates a so-called structural softening of the domain, due to local rotation of stresses when crossing a shear band (Vermeer and de Borst, 1984).

In natural rocks (e.g. fault gouges), the evolution of material properties with permanent deformation can be complex, with either strain-hardening or strain-softening processes that depend on a variety of parameters, such as fluids, confining pressure, strain rate and temperature. Various deformation-depending laws describe such evolving material properties (e.g. review by Lockner, 1995). Although our numerical code permits the implementation of a variety of laws very easily, we chose not to test them specifically in the present study, because of the large variety of, and poorly controlled, possible behaviours. However, we shall discuss their possible effect later on.

Despite Parovoz being a two-dimensional plane strain code, failure conditions are tested accounting for the three-dimensional distribution of stresses. Shear failure (mode II type) is accounted for by the Mohr–Coulomb criteria, and tensile failure is detected, when one or more stress components exceed the maximum tensile value given by So/tan(ϕ) (point where the yield envelope intersects with the horizontal normal stress axes in Mohr's circle). Therefore the numerical models can identify areas of extensional failure, but because the continuum of elements cannot split such as real mode I crack opening, we cannot model in detail the processes of tensile fractures. A number of studies show that in rocks, failure often occurs by a mixture of mode I and mode II styles at different scales (e.g. Scholtz, 1990; Lockner, 1995). In fact, White et al. (2004) compared models produced with FLAC2D and with a Particle Flow Code (using elastic particles joined by breakable elastic bonds) in a modelling study of mining-induced extensional fractures. These authors conclude that "FLAC2D models identified sites of high tension, whereas PFC models simulated the fracture process and showed that individual microfractures formed as a result of combined shear and tension, and macro-fractures propagated by the same basic mechanism".

Our modelling is not intended to reproduce the mechanism of fracturing (mode I vs. mode II); instead the numerical experiments were designed to identify where extension and tensile failures occur during the propagation of a main reverse fault at the Earth surface. In the experiments the size of the extensional domain remains small compared to the depth-extent of the main thrust-fault, and the strength of rocks at the topographic surface remains small compared with rocks located at deeper structural levels (pressure dependency of the failure yield). Therefore we suggest that the elasto-plastic models presented here should give a good first-order approximation of the surface areas that fail.

8.1. Model setup

The upper crust is modelled as a medium of 150 by 30 quadrilateral elements, corresponding to a total length of 15 km and a depth of 3 km for the reference experiment. The bottom base of the model is fixed vertically (free-slip condition). The surface

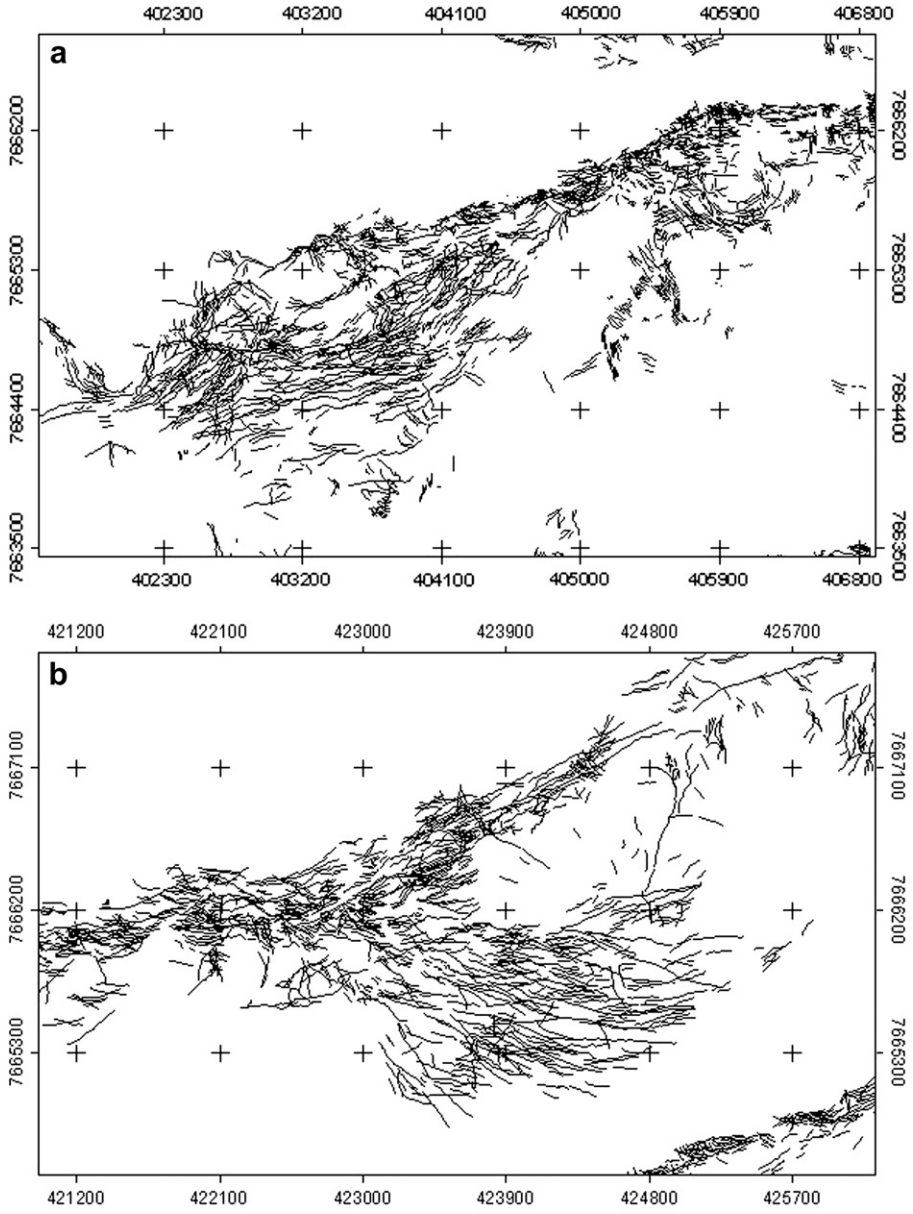

Fig. 10. (a) Map of the crack distribution at the western tip zone of Fault B. (b) Fanning geometry of the fracture network in the central part of Fault B. Distance between tick marks is 900 m.

is stress free and the lateral borders are free to slip vertically. The left border is fixed in the horizontal direction and a horizontal shortening is applied from the right border. Note that since the model accounts for a time-independent elasto-plastic rheology, deformation does not depend on the shortening velocity but only on the amount of shortening applied in the experiment. For a complete description of the mechanical and geometrical parameters introduced in the models, see Table 1. We insert a mechanical anisotropy in the models to simulate the existence of a pre-existing reverse fault zone, according to regional observations of reactivated Mesozoic faults. We varied the geometry of this pre-existing fault to see how this parameter influences the characteristics of superficial extension. The reference experiment (M1) considers a planar 50° dipping pre-existing fault extending to 3 km depth. Other experiments have been performed considering either a 6 km thick model (M2), or a pre-existing fault with listric geometry (M3, see Table 1).

In numerical experiments, the pre-existing fault zone is modelled by a 500 m thick layer having weaker mechanical properties than the surroundings. The internal friction angle of the intact rock is $\phi = 30°$, while the friction of the pre-existing fault zone is smaller, set to either 10° or 25° (M4, Table 1). Cohesion So was set to 1 MPa for both the "intact rock" and the "fault zone", except for model M5 where cohesion was equal to 10 MPa in the "intact" rock. These values correspond to common ranges in rock mechanics (see references in Ranalli, 1995; Reid et al., 2000), and are discussed later.

As shortening is applied in the numerical models, the pre-existing fault-ramp develops as a reverse fault zone. We look at the associated topography and superficial deformation as a function of the uplift accommodated by reverse-motion. We stop the experiments when maximum uplift reaches approximately 300 m, which corresponds to the largest uplifts observed in the Chuculay Fault System.

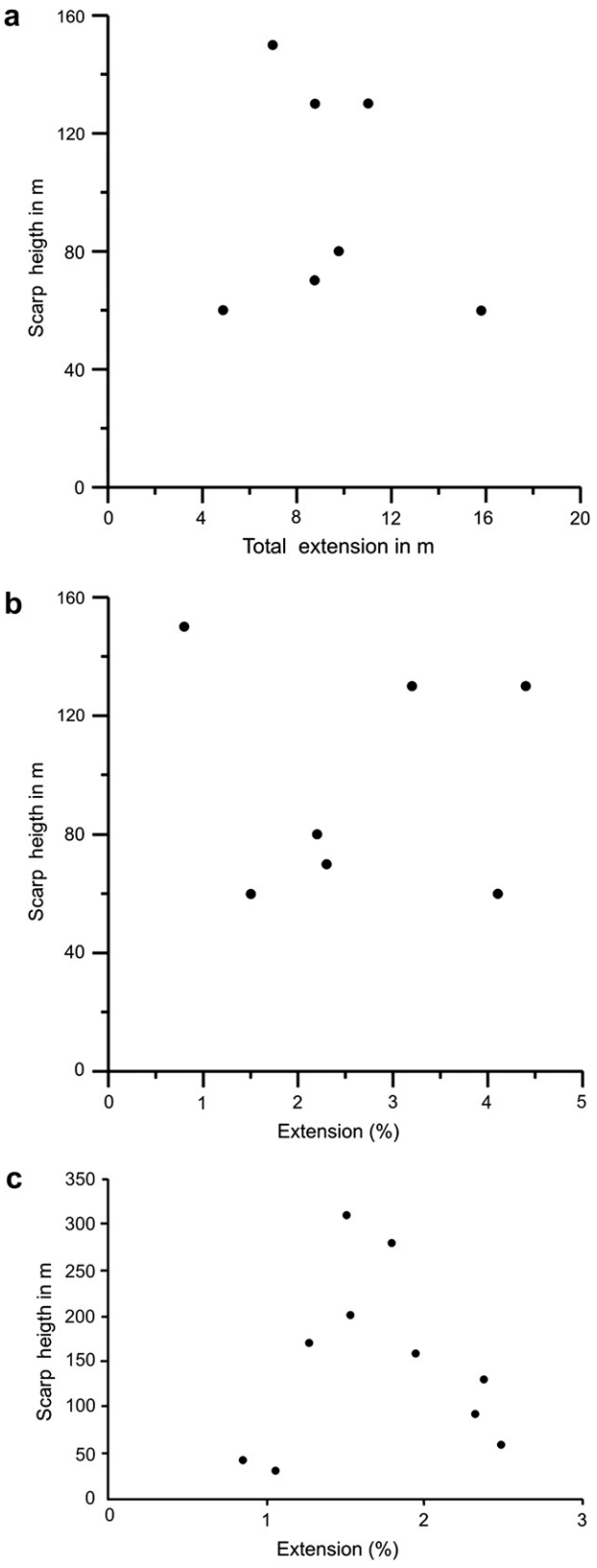

Fig. 11. (a) Height of scarp vs. total extension measured in the field transects. (b) Height of scarp vs. strain measured in the field transects. (c) Height of scarp vs. strain measured in the IKONOS image. There is poor correlation between scarp height and extension.

8.2. Reference model 1

This model is 15 km long and 3 km thick; the pre-existing fault extends from the base of the model to the surface with a constant 50° dip (planar fault). The model is progressively compressed from its right-hand side, and deformation concentrates along the pre-existing weak fault-ramp. Material is brought upwards by sliding along this fault-ramp, producing a scarp of 284 m height after 450 m of shortening. The reference model after 450 m of shortening is presented in Fig. 12: Fig. 12a–c displays topography, shear strain rate and shear stress invariants over the entire domain of the model, respectively. The upward motion is accommodated by a secondary fault zone that forms conjugate to the pre-existing one, and that initiates where the base of the model intersects the pre-existing weak zone. We observe that the entire 3 km thick layer of the model is tilted and flexed upwards above the pre-existing structure. Tilting is moderate (0.9° at the end of experiment) and occurs because the area located between the main reverse fault and the conjugate fault is not perfectly rigid as would be the case in kinematic models of this type.

8.3. Surface extension in reference model 1

Fig. 12d shows the orientation and relative magnitude of the eigenvectors of the stress tensor. Although the stress regime is essentially compressive within the models (most compressive stress axis, σ_1, is horizontal), the principal axes of the stress tensor rotate in the uplifted area, and values of the horizontal stress diminish enough for tension to occur close to the surface. Fig. 12e shows the orientation and relative magnitude of strain ellipses, and illustrates the superficial extensional deformation above the main scarp resulting from this tension. Fig. 12f shows areas that reach the Mohr–Coulomb shear failure criterion (in blue), at the given time-step corresponding to the end of the numerical experiment (no tensile failure occurs, see definition above). In fact, this figure plots "instantaneous" rupture that develops in such a way that different elements may fail at one time-step or the other, i.e. the total domain area that suffers plastic deformation during the experiment is larger than that represented in Fig. 12f. This figure shows that anelastic extensional zones deform the uplifted block over a distance about 2 km wide, extending from the fault scarp behind the hinge zone.

Fig. 13 shows the evolution of horizontal strain (ε_{xx}) close the main fault scarp as shortening increases. Horizontal extension is limited to the hanging wall block directly above the scarp, as observed in most of the Chuculay Fault System. After 100 m of shortening, fault scarp elevation is ~64 m and anelastic superficial horizontal extension affects a 1.5 km wide zone located in the hanging wall of the uplifted block (total extension as a function of scarp height is displayed in Fig. 14). Increase in scarp height by progressive shortening results in an increase of the superficial extension accommodated above the fault. In contrast, the width of the superficial stretched zone tends to remain constant with time only increasing from 1.5 to 2 km when the horizontal shortening increases from 100 to 400 m, and the vertical uplift from 64 to 280 m. This observation shows that surface extension is caused by horizontal stretching of the hanging wall in response to thrust motion and scarp uplift, and that its development is also bounded by the body forces in play.

8.4. Effect of fault geometry on the appearance of extensional structures

Deformation in the experiment depends on many parameters that are not known in the natural example: mechanical properties, such as friction and cohesion, and geometrical parameters, such

Table 1
Geometrical characteristics and mechanical parameters of the models

Model (reference)	Geometry		Elastic parameters		Fault rheology		Intact rock rheology	
	Depth (H, km)	Fault dip (α)	Young's modulus (E, Pa)	Poisson coefficient (ν)	Cohesion (So, MPa)	Friction angle (ϕ, degree)	Cohesion (So, MPa)	Friction angle (ϕ, degree)
1	3	50° (planar)	7.5×10^{10}	0.25	1	10	1	30
2	6	50° (planar)	7.5×10^{10}	0.25	1	10	1	30
3	3	Listric	7.5×10^{10}	0.25	1	10	1	30
4	3	50° (planar)	7.5×10^{10}	0.25	1	25	1	30
5	3	50° (planar)	7.5×10^{10}	0.25	1	10	10	30

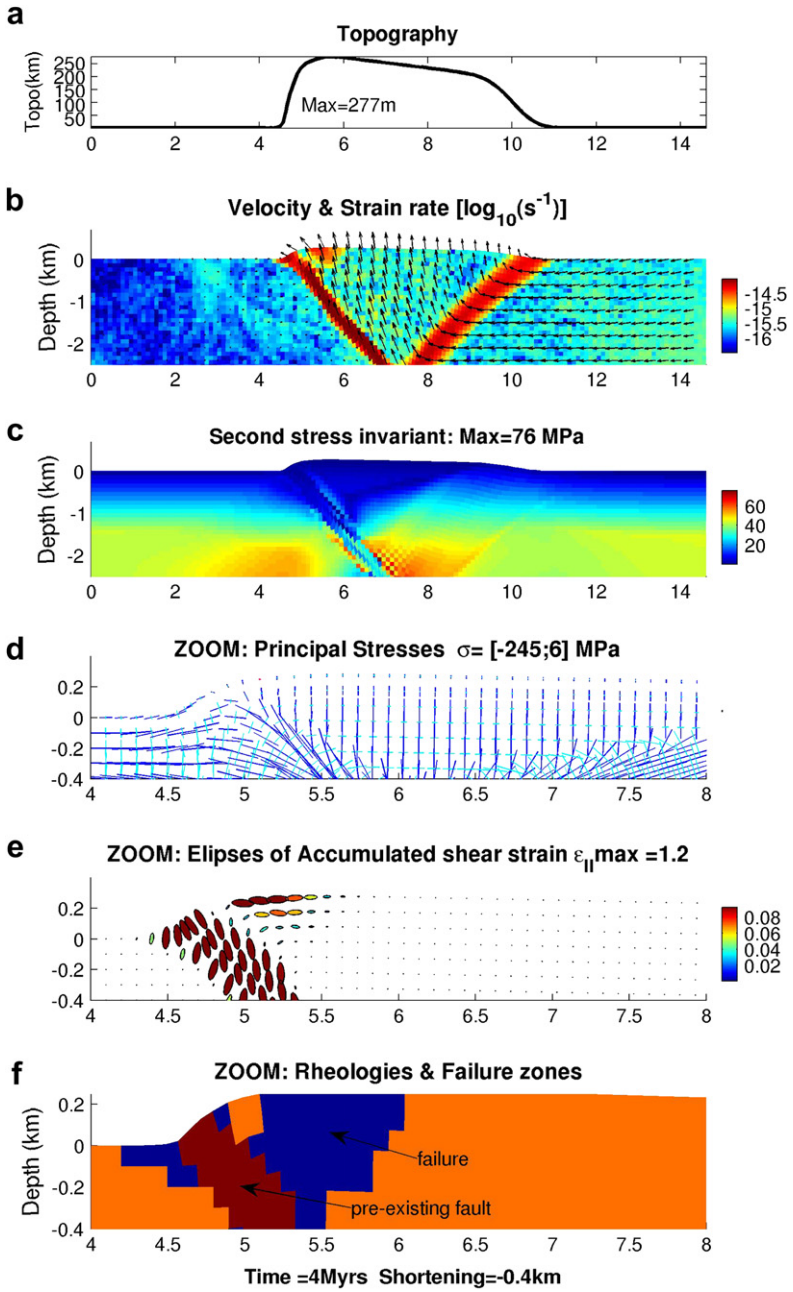

Fig. 12. Reference model 1 after 450 m of shortening. See text and Table 1 for boundary conditions and elastic parameters. (a) Topography, (b) second invariant of the deviatoric shear strain rate and velocity vectors, (c) second invariant of the deviatoric shear stress, red colour corresponds to highest values. (d–f) Zooms close to the fault scarp (d) crosses mark the principal stress axes, dark blue and light blue bars corresponding to the larger and smaller compressive stress, respectively. Note the diminution of the horizontal stress inside the tilted block, (e) ellipses of the accumulated strain, indicating horizontal elongations at the scarp tip, and (f) areas of plastic deformation at the time-step corresponding to the end of experiment (in blue) and pre-existing rheological weak zone (in brown).

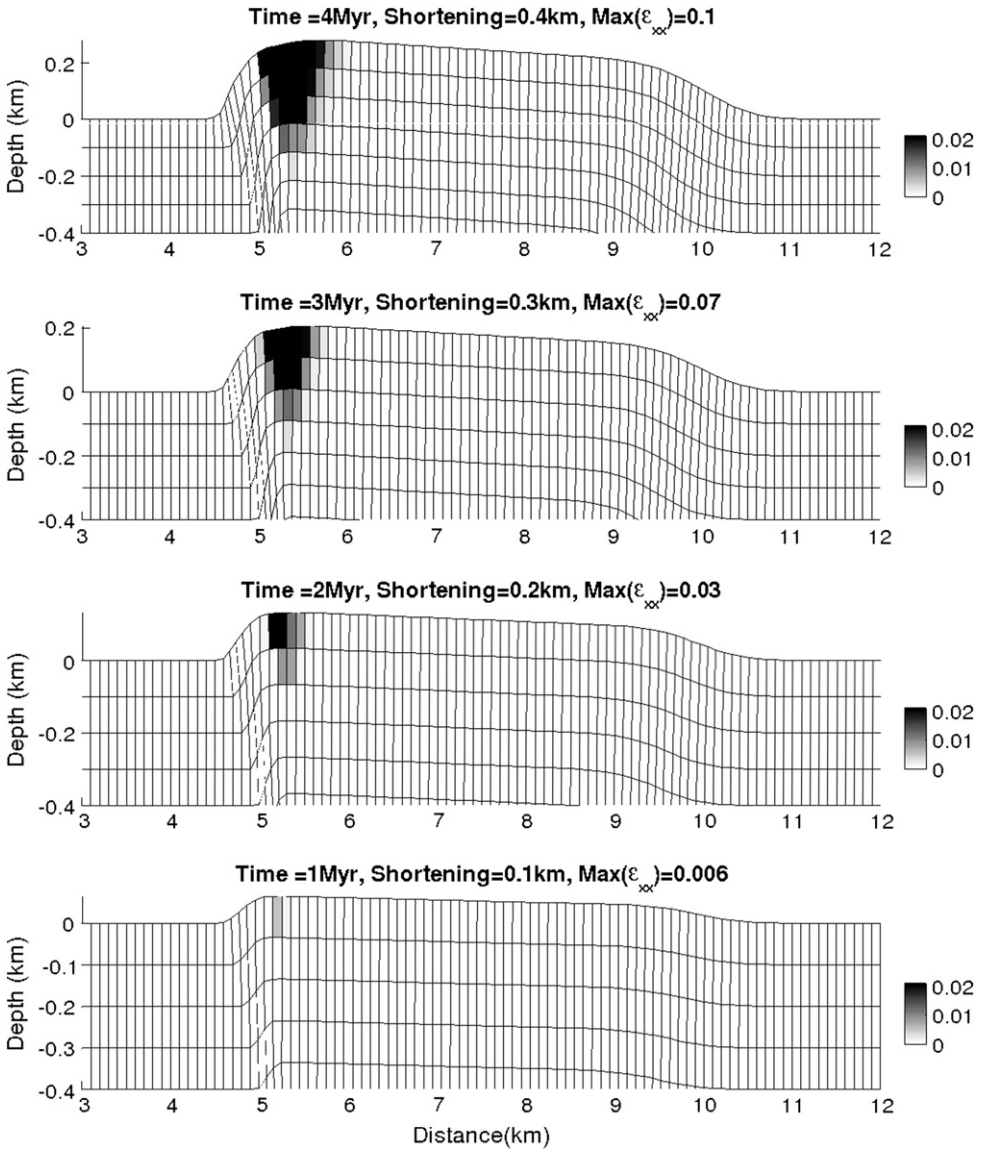

Fig. 13. Evolution of the horizontal strain ε_{xx} close the main fault scarp for the reference experiment M1. Black values correspond to $\varepsilon_{xx} > 2\%$, maximum values given in each figure title.

as the basal depth and the dip of the pre-existing fault. To begin, we changed the depth of the model and the shape of the fault to see how these geometrical parameters influence the appearance of superficial extension.

Model 2 is similar to the reference model, except that the thickness of the shortening layer has been increased to 6 km. The resulting uplifted block is approximately two times wider than in the reference model 1 (Fig. 15a), as it should be proportional to its depth (e.g. Jaeger and Cook, 1979; Liu and Dixon, 1995; Gerbault et al., 1998). For the same scarp height, the width of the extensional zone above the scarp is approximately two times larger than in the reference experiment (Fig. 14b). Thus, this model confirms that the width of the extensional zone depends on the location of the horizontal detachment at depth. Although superficial extension is more diffuse, the amount of extension is smaller than in model 1 (Fig. 14a). This is because hanging wall uplift at the surface develops only when the entire extent of the pre-existing fault zone slides plastically, down to 6 km instead of 3 km depth. In order to reach a similar scarp height, greater shortening is thus required, to generate the greater stresses that enable rupture at 6 km instead of 3 km depth. Consequently, superficial plastic deformation is also delayed, i.e. tensile structures form later than in experiment 1.

In model 3, the effect of a pre-existing listric fault geometry is tested. As the dip of this pre-existing fault progressively decreases from 50° to 0° at 3 km depth, its conjugate fault does not significantly develop because there is no localized geometrical discontinuity at depth (Fig. 15b). The tilting of the uplifted block is larger (2.5° vs. 0.9° in the reference model 1 for a 300 m high scarp; see Table 1). Larger tilting is necessary here to accommodate a similar scarp height, it coincides with the observed field geometry. In this model, surface extension appears later than in the two previous models: surface extension in the hanging wall block only appears after the scarp is 120 m high. Even for a larger scarp height, extension remains localized in a narrower zone above the scarp ($\sim$1 km wide vs. 2 km for the reference experiment, Fig. 14a and b).

Comparison between these first three experiments shows that the superficial expression of the reverse faults depends on the geometry of the pre-existing fault and on the depth of the detachment zone. More contrasting topographic differences arise when

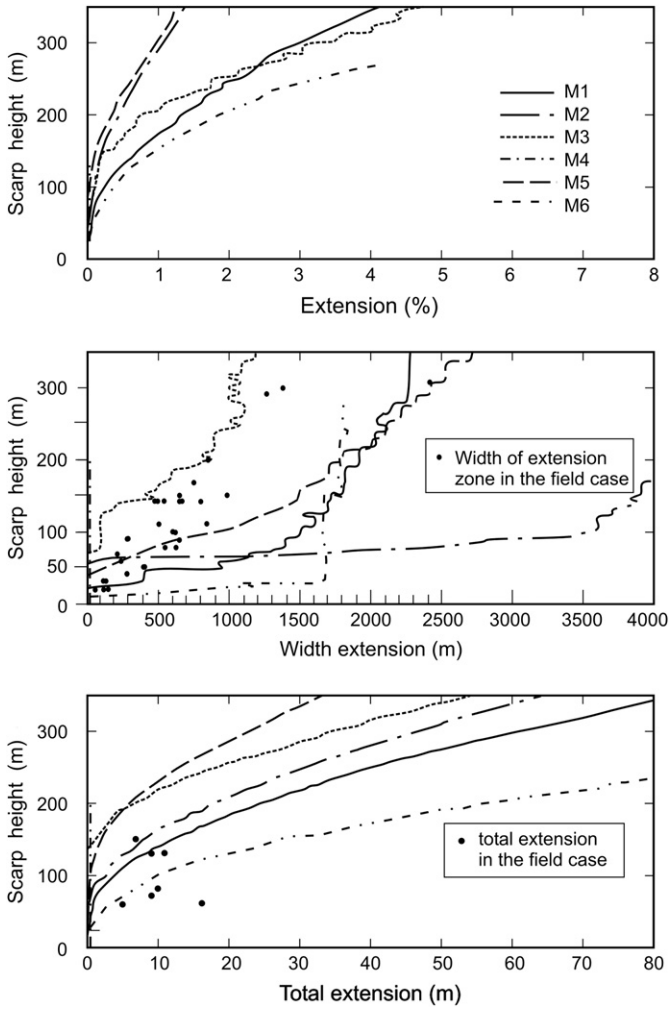

Fig. 14. Scarp height for all six models, as a function of (a) horizontal extension at the surface, measured as the sum of the elementary horizontal strain multiplied by elementary width ($dx(i)$), and divided by the total "width" of extension ($\sum(\varepsilon_{xx}(i)dx(i))$/ width, for $\varepsilon_{xx}(i) > 0$). (b) Scarp height plotted against the width of extension, measured as the total width of the elements under extension ("width" $= \sum dx(i)$, for $\varepsilon_{xx}(i) > 0$). Sharp steps on profiles correspond to the inclusion (or exclusion) of elements (100 m wide) of positive ε_{xx}.

the fault is either planar or listric; the latter does not produce the pop-up structure which is characteristic of model 1 and model 2. Furthermore, the experiments show that the width of the area in extension depends on the localization of the detachment zone at depth and on the fault profile. A deeper localization of the detachment zone as in model 2 favors a wider extensional area, whereas the amount of extension is significantly smaller (about 1% vs. 3% for the 3 km deep planar fault of model 1). On the other hand, a listric fault geometry as in model 3, favors a narrower area of extension than planar faults. However, the order of magnitude of superficial horizontal extension, expressed in per cent, is similar to that of model 1, with about 3% extension for a 300 m high scarp. This indicates that the amount of total extension depends on both geometrical parameters of the pre-existing fault.

8.5. Mechanical parameters controlling surface extension

In the following models we tested different mechanical parameters to assess the relationship between extension on top of the reverse fault and mechanical fault properties.

In model 4 (Fig. 16a), the internal friction angle of the pre-existing fault zone is increased compared to experiment 1 ($\phi_f = 25°$ vs. $\phi_f = 10°$ in M1, Table 1). Other parameters remain unchanged. In this model, the required horizontal compression to produce equivalent height of the hanging wall is larger than in model 1, since the pre-existing fault is stronger. No extension is observed on top of the reverse fault. This experiment indicates that the pre-existing fault must be sufficiently weak in order to release stresses and generate extension on top of the reverse-fault scarp.

In model 5, we increase the cohesion of the intact rock to 10 MPa, instead of 1 MPa as in the previous experiments. Other parameters remain same as in the reference model (Table 1). In this model, although some minor extension appears as soon as a modest scarp has formed (as in experiment 1), the amount of extension becomes significant (larger than 10 m) for scarp heights greater than 230 m vs. 140 m for the reference model 1. Increasing cohesion strengthens superficial rocks and delays the occurrence of anelastic deformation at the surface. The total amount of extension accommodated in the stretched area is approximately three times smaller than in the reference model, for a scarp height of 300 m (Fig. 14a). The width of the stretched zone, in contrast, does not appear to depend much on cohesion (Fig. 14b).

Some softening of friction and cohesion as rocks fail, especially when forming tensile mode I cracks, should increase the development of superficial tension. However, to our knowledge, strain-softening properties of rocks, e.g. the evolution of mechanical properties with failure, still lack a precise description that can account for the observed variety of behaviours. We ran an additional model, not shown here, in which cohesion and friction were empirically reduced to 0.01 MPa and 15°, respectively, as plastic shear strain reached 0.01. The model indeed develops about 10 m greater amount of extension over a width of about 1800 m for scarp heights below 100 m. However, for greater scarp heights, superficial extension becomes equivalent to model 1, indicating that softening of rock properties indeed enhances small scale structures, but does not significantly increase total amounts of extension.

9. Discussion

9.1. Contrasting the field case with models

The purpose of the mechanical models in this paper is not to simulate the exact geometry of the extensional structures documented in the field but to contribute to an understanding of the basic mechanical processes and the kinematic regime that might have influenced their development. In this sense all mechanical models show basically the same overall structure as in the field: a concentration of anelastic superficial extension predominantly at the top, rather than on the forelimbs, of the scarps. The second order features – width of the zone of extension, density of the fractures – are not significant to extract fundamental physical conclusions from the models; they may be well below the resolution of the mechanical models. However, we use these features as second order indicators of the mechanical and geometrical characteristics of the pre-existing reverse faults of the natural case.

The field case reveals that extension appears as soon as the shortening produces a modest scarp of just 20 m high. Increasing scarp height produces a widening of the extension zone above the reverse fault, but we do not observe the same correlation between scarp height and the extensional strain. In the natural case, extension expressed in per cent shows a poor correlation with scarp height; mainly because of two deviations present in the point distribution: 4% of extension for a 60 m height scarp, and 1% of extension for a 145 m height scarp. These deviations from the generally positive correlation can be explained by variation in the grade of

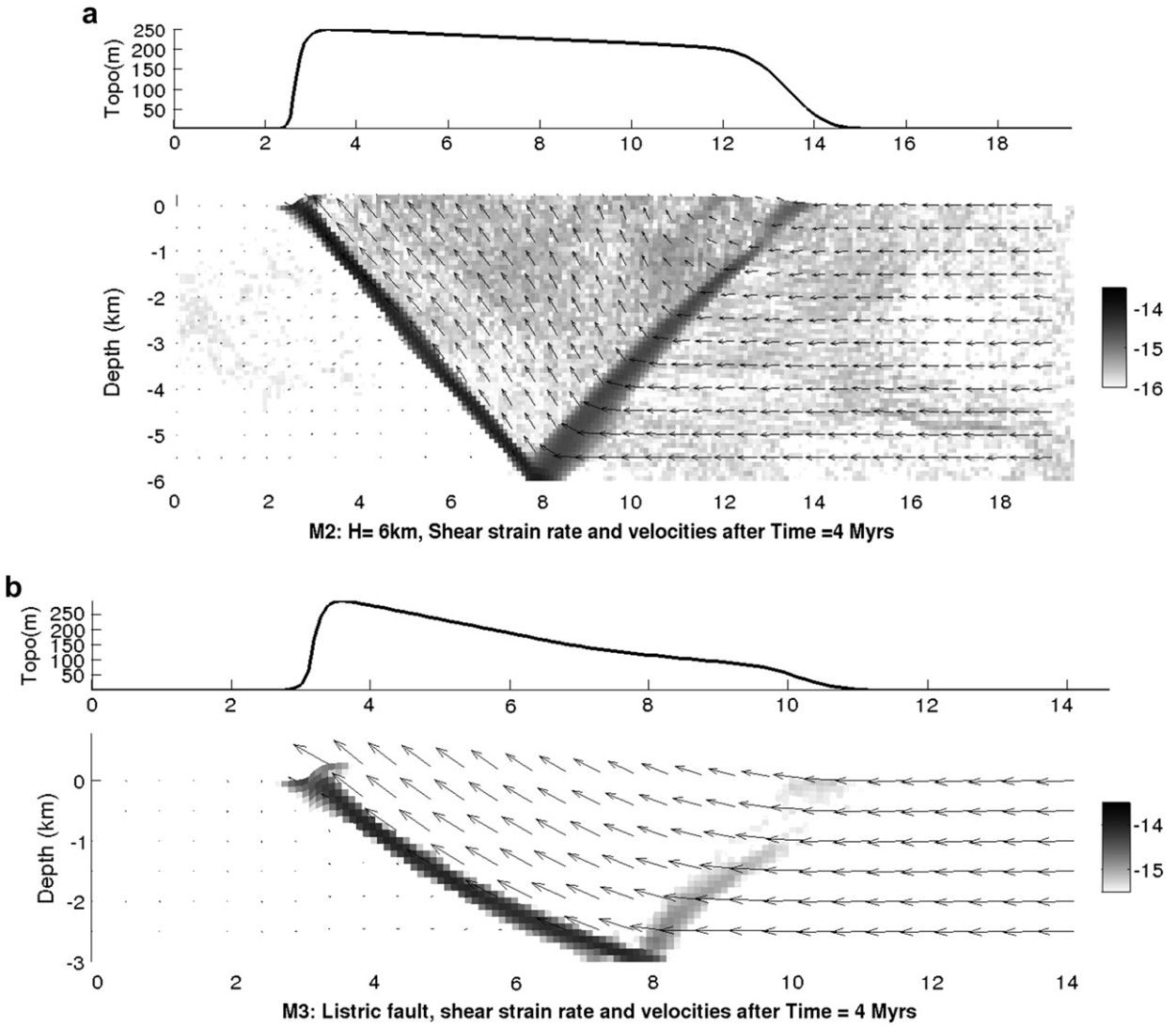

Fig. 15. Models testing the geometrical properties (see Table 1). Topography, second invariant of the shear strain rate and velocities vectors. (a) Model 2 extends down to 6 km depth. The width of the uplifted thrust is greater but the scarp uplift remains similar. (b) Model 3 accounts for a listric fault. The uplifted thrust does not require the development of a conjugate fault.

weathering of the country rocks. In the first case (4%) the country rocks are formed by volcanic rocks with strong meteoric alteration, whereas in the second case (1%) they represent non-altered plutonic rocks. Variation of the weathering grade should change the mechanical properties of these country rocks. Comparison between total extension and scarp height in the natural case and in the models shows that for scarp height $<$100 m, total strain in the field is larger than total strain in the models (Fig. 14c), and for scarp height $>$100 m, total strain in the field case is similar to the total strain in the models (see below).

Numerical models show that the localization of the extensional zone that develops on top of the reverse-fault scarps depends directly on the following mechanical properties: (1) the cohesion (So) of the material, which controls its rupture close to the topographic surface where pressure is negligible in the yield stress criterion, and (2) the weakness of the fault zone as expressed by the internal frictional angle ($\tan\phi = \mu$), and which controls the ability to release compressive stresses in the up-thrust block. A higher value of cohesion of the intact rocks delays fracture appearance but does not exert a fundamental control on the width of the fracture zone on top of the scarp. When the fault is strong ($\phi = 30$–25°), compression prevails in the entire model and surface extension does not develop. In order to produce extension on top of the scarps, the master fault has to be weak.

Comparison of extension and topography produced in the numerical experiments and in the natural field example suggests that the Chuculay Fault System is dominated by weak reverse faults. Field observations show that the scarps of the Chuculay Fault System were progressively created in different events of slip. Repeated slip events should result in a pronounced weakening of the rocks in the fault zone. By this process, internal frictional angle and cohesion in the fault zone should progressively decrease. Numerical models show a difference when intact rock cohesion is increased by a factor 10 (model 5), producing lower extension. Field mapping shows that the amount of extension depends on the weathering grade of the rocks which in turn influences the mechanical properties of the stretched zone.

The models suggest that distribution of extension at the surface of the hanging wall also depends on the geometrical parameters of the fault, i.e. depth of the detachment zone and fault plane geometry. A deeper detachment (model 2) generates a wider area of extension, but produces a lesser amount of total extension. The

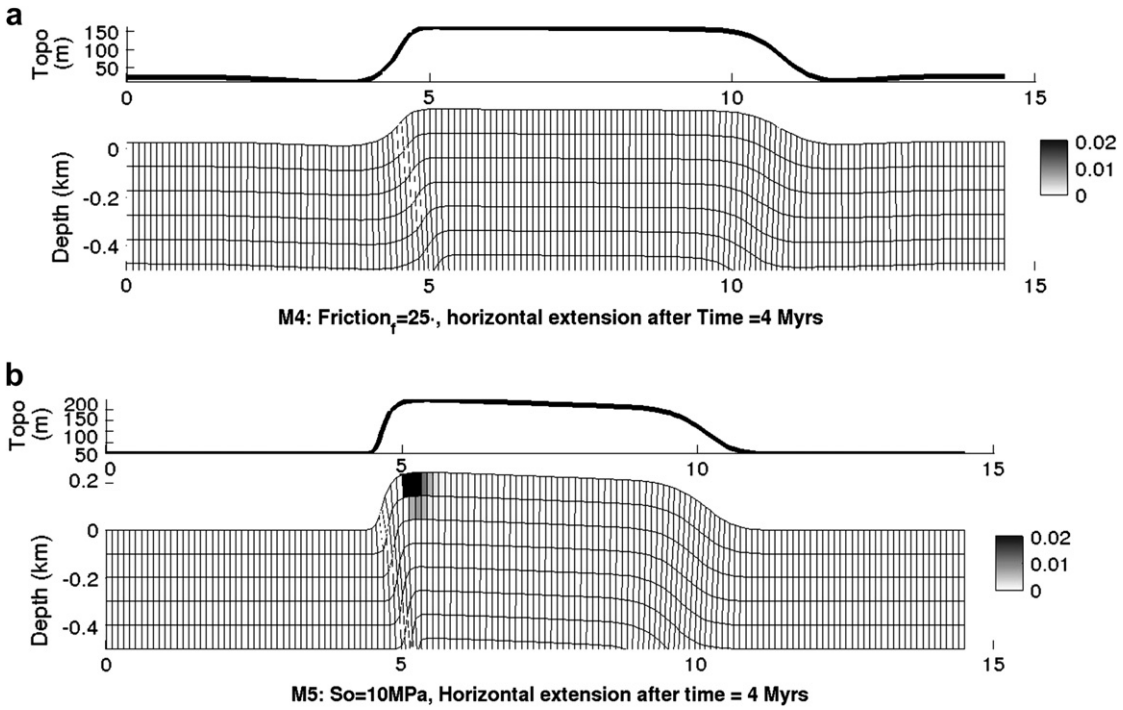

Fig. 16. Effects of rupture parameters on surface extension. Topography and horizontal extension ε_{xx} for models after 4 Myrs. (a) M4 has a pre-existing fault friction of 25° (instead of 10° in M1). No extension develops, but topographic uplift also occurs beyond the thrusted block, illustrating more uniform deformation. (b) M5 has a cohesion So = 10 MPa (instead of 1 MPa in M1). Compare with figure M2.

topography produced by the listric numerical experiment is similar to that observed in the field, suggesting that the reverse faults of the Chuculay System have a listric geometry. This suggestion coincides with regional field data indicating that the dip of the E–W reverse faults diminished with depth. Reactivation of listric faults better explains the tilting of the topographic surface of the hanging wall of the Chuculay System. Furthermore, this listric geometry correlates better with the absence of conjugate faults in the Chuculay Fault System, and favors a concentration of fractures at the top of the scarp. However, the width of the extension zone and the total strain in the listric numerical model shows some differences with the field case. In the listric numerical model (M3), scarp height needs to be higher than in the field case to produce a "visible" extension (Fig. 14b).

In fact, in all our numerical models, superficial horizontal stretching appears later than in the natural example. Extension in the models initiates only when the height of the scarp reaches a value ranging between 50 and 120 m. This result follows from the method used to model the master thrust-fault as a relatively wide plastic zone. Horizontal stretching appears sooner if we account for a thinner fault zone. In model 6 we tested this effect. This model accounts for a 250 m wide pre-existing fault zone instead of 500 m as in model 1 (Fig. 14): it develops superficial extension at low scarp heights, but reaches equivalent amounts of extension for heights greater than 100 m. Another possible reason for the discrepancy between nature and numerical models is that the Chuculay scarps do not precisely correspond to fault-bend-folds, which is discussed in Section 9.2. Also, the strength of the fault zone and the cohesion of rocks may be smaller in the natural case than in the models. Finally, the amount of extension produced in the superficial elements of the numerical model depends on the spatial resolution of each grid-element, which was here equal to 100 m. For the spatial dimensions considered in the models, this resolution is sufficient in the sense that the mechanical equations of the code are precisely written with the small deformation formulation. However, in the field case, superficial rocks are not divided in such continuum blocks and one can record greater extension at the small scale. Real mode I crack opening reduces cohesion and frictional conditions for failure, whereas in the present models, these parameters are held constant through time. Numerical models accounting for strain-softening, or other codes able to reproduce mode I failure (like PFC, see for example White et al., 2004), should be able to produce slightly greater amounts of superficial extension, especially for small scarp heights.

9.2. Extension mechanism

In the reference model and in the listric model, velocity vectors diverge in the forelimb of the scarp (Fig. 17). This demonstrates that when the scarp starts to form, the forelimb of the scarp experiences a counter-clockwise rotation about a horizontal axis. In Fig. 13 this rotation is observed by the progressive tilting of the vertical lines outwards of the scarp. We suggest that rotation of the forelimb is the expression of folding of the hanging wall when the fault emerges and starts to propagate parallel to the topographic surface. Hanging wall folding produces a surface parallel stretching over the scarp; in an initial stage stretching generates elastic strain until the failure condition is reached on top of the scarp.

Kinematic models of similar fault-bend-folds show that extension is concentrated in the forelimb, which is not the case documented in the field or in the mechanical models. This raises the question of whether the extensional structures of the Chuculay Fault System can be interpreted in terms of a kinematic model such as fault-bend or fault-propagation folding. Relationship at the tip lines suggests, at very least, that they propagate laterally as fault-propagation folds. At their centres, where the faults have the highest relief, they may have had an early history of fault-propagation folding, but we suggest that the faults must have rapidly breached the surface and accrued significant subsequent slip and folding as fault-bend folds. In general, however, kinematic

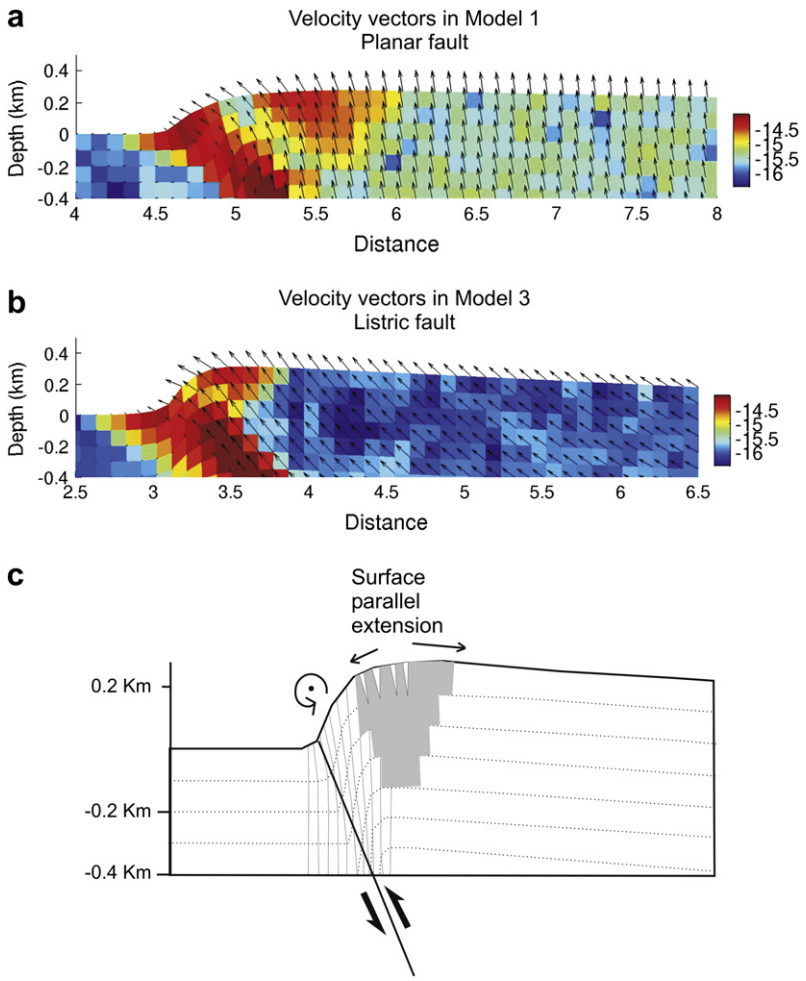

Fig. 17. Zoom on tip zone of models 1 and 3 showing the velocity field; note the divergence of the velocity vectors close to the scarp. Extension is produced by folding of the hanging wall close to the scarp as shown in the cartoon. Colours in elements represent the shear strain rate (second invariant), with a palette in units of log 10 (s^{-1}). Greatest shear strain is shown in red. As a dynamic feature of the models, the reference value may slightly vary from one time-step to the other according to local accelerations. In this snapshot of model 1 (a) for example, the pop-up block is experiencing internal deformation (more greenish colour), whereas on average it will take a bluish colour similar to the snapshot of model 3(b). (For interpretation of the references to colour in this figure legend, the reader is referred to the Web version of this article.)

models cannot duplicate the fine scale structural detail documented here.

Acknowledgments

This work has been funded by the Fondecyt project 1040389 (GG) and by the French-Chile Cooperation Program Ecos-Conicyt CU04. Mecesup program funded the Ph.D. fellowship to D. Carrizo. Allmendinger's work is supported by the National Science Foundation Grant EAR-0087431. We thank the logistic support provided for the Universidad Católica del Norte (Chile). We would like to express our thanks to reviewers Paul Bons (Ebbehard Karl Univesity of Tübingen) and Joao Hippert (Editor JSG) for important comments and suggestions that significantly improved the quality of this contribution.

References

Allmendinger, R., 1998. Inverse and forward numerical modeling of trishear fault-propagation folds. Tectonics 17, 640–656.

Allmendinger, R., Gonzalez, G., Yu, J., Hoke, G., Isacks, B., 2005. Trench-parallel shortening in the northern Chilean forearc: tectonic and climatic implications. Geological Society of America Bulletin 117, 89–104.

Anderson, E.M., 1951. The Dynamics of Faulting and Dike Formation. Oliver and Boyd, Edinburgh.

Cardozo, N., Bawa-Bhalla, K., Zehnder, A., Allmendinger, R., 2003. Mechanical models of fault propagation folds and comparison to the trishear kinematic model. Journal of Structural Geology 25, 1–18.

Carrizo, D., González, G., Dunai, T., 2008. Constricción neógena en la Cordillera de la Costa, norte de Chile: neotectónica y datación de superfi cies con $_{21}$Ne cosmogénico. Revista Geológica de Chile 35 (1), 1–38 (Enero, 2008).

Comte, D., Dorbath, L., Pardo, M., Monfret, T., Haessler, H., Rivera, L., Frogneux, M., Glass, B., Meneses, C., 1999. A double-layered seismic zone in Arica, northern Chile. Geophysical Research Letters 26, 1965–1968.

Cundall, P., Board, M., 1988. A microcomputer program for modelling large-strain plasticity problems. Numerical Methods in Geomechanics 6, 2101–2108.

Dahlen, F.A., 1984. Noncohesive critical Coulomb wedges: an exact solution. Journal of Geophysical Research 89, 10125–10133.

Delouis, B., Cisternas, A., Dorbath, L., Rivera, L., Kausel, E., 1996. The Andean subduction zone between 22 S and 24 S (northern Chile): precise geometry and states of stress. Tectonophysics 259, 81–100.

Dunai, T., González, G., Larre, J.J., 2005. Oligocene–Miocene age of aridity in the Atacama Desert revealed by exposure dating of erosion sensitive landforms. Geology 33, 321–324.

Finch, E., Hardy, S., Gawthorpe, R., 2003. Discrete element modelling of contractional fault-propagation folding above rigid basement fault blocks. Journal of Structural Geology 25, 515–528.

García, F., 1967. Geología del Norte Grande de Chile. In: Paper Presented at Simposium sobre el Geosinclinal Andino. Societe Geologia de Chile, Santiago.

Gerbault, M., Poliakov, A., Daignieres, M., 1998. Prediction of faulting from the theories of elasticity and plasticity: what are the limits? Journal of Structural Geology 20, 301–320.

González, G., Cembrano, J., Carrizo, D., Macci, A., Schneider, H., 2003. Link between forearc tectonics and Pliocene-quaternary deformation of the Coastal Cordillera, northern Chile. Journal of South American Earth Sciences 18, 321–342.

Hafner, W., 1951. Stress distributions and faulting. Geological Society of America Bulletin 62, 373–398.
Hancock, P., 1985. Brittle microtectonics: principles and practice. Journal of Structural Geology 7, 437–458.
Healy, D., Yielding, G., Kusznir, N., 2004. Fracture prediction for the 1980 El Asnam, Algeria earthquake via elastic dislocation modeling. Tectonics 23, doi:10.1029/2003TC001575 TC6005.
Hilley, G., Arrowsmith, R., Amoroso, L., 2001. Interaction between normal faults and fractures and fault scarp morphology. Geophysical Research Letters 28, 3777–3780.
Hobbs, B.E., Ord, A., 1989. Numerical simulation of shear band formation in frictional–dilational material. Ingenieur Archives 59, 209–220.
Jaeger, J.C., Cook, N.G.W., 1979. Fundamentals of Rock Mechanics. Methuen and Co., London.
King, G.C.P., Vita-Finzi, C., 1980. Active folding in the Algerian earthquake of 10 October 1980. Nature 292, 22–26.
Klinger, Y., Xu, X., Tapponnier, P., Van der Woerd, J., Lasserre, C., King, G., October 2005. High-resolution satellite imagery mapping of the surface rupture and slip distribution of the $M_w \sim 7.8$, 14 November 2001 Kokoxili earthquake, Kunlun Fault, Northern Tibet, China. Bulletin of the Seismological Society of America 95, 1970–1987.
Liu, S., Dixon, J., 1995. Localization of duplex thrust-ramps by buckling: analog and numerical modelling. Journal of Structural Geology 17, 875–886.
Lockner, D.A., 1995. Rock failure. In: Ahrens, T.J. (Ed.), Rock Physics and Phase Relations: A Handbook of Physical Constants. American Geophysical Union, pp. 127–147 (AGU Reference Shelf 3).
Malavieille, J., 1984. Modelisation experimentale des chevauchements imbriqués: application aux chaînes de montagnes. Bulletin Societé Géologique de France 7, 129–138.
Martel, S., Langley, J., 2006. Propagation of normal faults to the surface in basalt, Koae fault system, Hawaii. Journal of Structural Geology 28, 2123–2143.
Mitra, S., Islam, Q.T., 1994. Experimental (clay) models of inversion structures. Tectonophysics 230, 211–222.
Philip, H., Meghraoui, M., 1983. Structural analysis and interpretation of the surface deformations of the El Asnam earthquake of October 10, 1980. Tectonics 2, 17–49.
Poliakov, A., Podladchikov, Y., 1992. Diapirism and topography. Geophysical Journal International 109, 553–564.
Rajendran, K., Rajendran, C.P., Thakkar, M., Tuttle, M.P., 2001. The 2001 Kutch (Bhuj) earthquake: coseismic surface features and their significance. Current Science 80 (11), 1397–1401.
Ranalli, G., 1995. Rheology of the Earth, second ed. Chapman & Hall, 413 pp.
Reid, M.E., Christian, S.B., Brien, D.L., 2000. Gravitational stability of 3-dimensional stratovolcano edifices. Journal of Geophysical Research 105 (B3), 6043–6056.
Rudnicki, J.W., Rice, J.R., 1975. Conditions for the localization of deformation in pressure-sensitive materials. Journal of the Mechanics and Physics of Solids 23, 371–394.
Sassi, W., Faure, J.-L., 1997. Role of faults and layer interfaces on the spatial variation of stress regimes in basins: inferences from numerical modelling. Tectonophysics 266, 101–119.
Scholtz, C.H., 1990. The Mechanics of Earthquakes and Faulting. Cambridge University Press.
Stockmal, G.S., 1983. Modeling of large-scale accretionary wedge deformation. Journal of Geophysical Research 88, 8271–8287.
Tchalenko, J.S., 1970. Similarities between shear zones of different magnitudes. Geological Society of America Bulletin 81, 1625–1640.
Tichelaar, B.W., Ruff, L.J., 1991. Seismic coupling along the Chilean subduction zone. Journal of Geophysical Research 96, 11997–12022.
Tucker, M.E., 1978. Gypsum crusts (gypcrete) and patterned ground from northern Iraq. Zeitschrift für Geomorphologie 22, 89–100.
Vermeer, P.A., de Borst, R., 1984. Non-associated plasticity for soils, concrete and rocks. Heron 29, 1–75. Stevin-Laboratory of Civil Engineering, University of Technology, Delft and Institute TNO for Building Materials and Building Structures, Rijswijk, The Netherlands.
White, B.G., Larson, M.K., Iverson, S.R., 2004. Origin of mining-induced fractures through macroscale distortion. In: Gulf Rocks 2004: Rock Mechanics Across Borders and Disciplines, Proceedings of the Sixth North American Rock Mechanics Conference, June 5–10, 2004, Houston, Texas. Report No. ARMA/NARMS 04-569.
Yielding, G., Jackson, J.A., King, G.C.P., Sinvhal, H., Vita-Finzi, C., Wood, R.M., 1981. Relations between surface deformation, fault geometry, seismicity, and rupture characteristic during the El Asnam (Algeria) earthquake of 10 October 1980. Earth and Planetary Science Letters 56, 287–304.